HHS Public Access

Author manuscript

*Nat Nanotechnol*. Author manuscript; available in PMC 2018 October 30.

Published in final edited form as:

*Nat Nanotechnol*. 2018 June ; 13(6): 512–519. doi:10.1038/s41565-018-0111-5.

# Multifunctional biophotonic nanostructures inspired by longtail glasswing butterfly for medical devices

**Vinayak Narasimhan**[1,†], **Radwanul Hasan Siddique**[1,†], **Jeong Oen Lee**[1,2], **Shailabh Kumar**[1], **Blaise Ndjamen**[1], **Juan Du**[3], **Natalie Hong**[1], **David Sretavan**[3,*], and **Hyuck Choo**[1,2,*]

[1]Department of Medical Engineering, California Institute of Technology, 1200 E. California Blvd., MC 136-93, Pasadena, California 91125, USA.

[2]Department of Electrical Engineering, California Institute of Technology, 1200 E. California Blvd., MC 136-93, Pasadena, California 91125, USA.

[3]Department of Ophthalmology, University of California, San Francisco, San Francisco, CA 94143, USA.

## Abstract

Numerous living organisms possess biophotonic nanostructures that provide coloration and other diverse functions for survival. While such structures have been actively studied and replicated in the laboratory, it remains unclear whether they can be used for biomedical applications. Here we show a transparent photonic nanostructure inspired by the longtail glasswing (*Chorinea faunus*) butterfly and demonstrate its use in intraocular pressure (IOP) sensors *in vivo*. We exploit the phase separation between two immiscible polymers (poly(methyl methacrylate) and polystyrene) to form nanostructured features on top of a $Si_3N_4$ substrate. The membrane thus formed shows good angle-independent white light transmission, strong hydrophilicity and anti-biofouling properties that prevent adhesion of proteins, bacteria, and eukaryotic cells. We then developed a microscale implantable IOP sensor using our photonic membrane as an optomechanical sensing element. Finally, we performed *in vivo* testing on New Zealand white rabbits and show that our



[*]These authors are co-corresponding authors. hchoo@caltech.edu, David.Sretavan@ucsf.edu.
[†]These authors contributed equally to this work.

**Author Contributions**

V.N., R.H.S., and H.C. conceived the study. V.N. and R.H.S. designed the analyses while supervised by H.C. R.H.S. conducted the microscopy and spectroscopy of the longtail glasswing butterfly. R.H.S. conducted the simulations and numerical analysis. V.N. and R.H.S. fabricated and characterised the nanostructured $Si_3N_4$-membrane samples. V.N., R.H.S., S.K. and N.H. conducted the *in vitro* tests. V.N., J.L. and R.H.S. fabricated and characterised the benchtop IOP sensors. V.N., J.L. and J.D. performed the *in vivo* experiments under the supervision of D.S. V.N. and B.N. conducted the biocompatibility experiments of the *in vivo* IOP sensors. V.N., R.H.S. and H.C. co-wrote the manuscript with assistance from D.S. All authors discussed the results and commented on the manuscript.

**Data availability**

The data that support the plots within this paper and other finding of this study are available from the corresponding author upon reasonable request.

Supplementary information is available in the online version of the paper.

**Competing financial interests**

The authors declare no competing financial interests.

device reduces the mean IOP measurement variation compared to conventional rebound tonometry without signs of inflammation.

An estimated 8–10% of Americans and 5–6% of people in other developed nations depend on implantable medical devices to support or rebuild organs and other functions of the body during their lifetime[1,2]. Consequently, efforts to develop medical implant technologies are increasing. A major deterrent to these efforts, however, has been the requirement to incorporate multiple functionalities within a tightly constrained footprint while ensuring acceptable *in vivo* performance and reliability[3–6].Inspiration for engineering multifunctional surfaces is often drawn from nature, which boasts a plethora of nanostructures with a wide array of desirable properties[4–8]. For example, vertically-tapered needle-like nanostructures found on the wings of insects exhibit multifunctionality including omnidirectional antireflection, self-cleaning, antifouling, and bactericidal properties[9–13]. Such properties may prove to be advantageous for biomedical applications such as *in vivo* sensing, imaging, and stimulation.

Herein, we seek inspiration from the multifunctional biophotonic nanostructures found on the transparent wings of the longtail glasswing (*Chorinea faunus*) butterfly to advance the versatility of micro-optical implants whose practical use is often limited by the angle dependency of sensing and readout processes[14,15] as well as short- and long-term biofouling[15–17]. We characterised in detail the surface and optical properties of the short-range-ordered nanostructures found on the *C. faunus* butterfly wings that could overcome the shortcomings of micro-optical implants. We reveal that *C. faunus* relies on relatively moderate-aspect-ratio (aspect-ratio ≈ 1) chitin nanostructures to produce (1) transparency that is a unique combination of wavelength-selective anti-reflection and angle-independent transmission resulting from isotropic Mie scattering, and (2) antifouling properties through disruption of cellular growth similar to that observed on high-aspect-ratio (aspect-ratio > 1) structures found in nature[12,13]. Drawing our inspiration from the *C. faunus* nanostructures, we created low-aspect-ratio (aspect-ratio < 1) bio-inspired nanostructures on freestanding $Si_3N_4$-membranes using a highly-scalable phase-separation-based polymer-assembly process. Unlike previous high-aspect-ratio bio-inspired nanostructures replicating antireflection[9,12,13], we engineered the pseudo-periodic arrangement and dimensions of nanostructures to control isotropic scattering and enhance omnidirectional optical transmission, which could benefit sensing and readout processes of micro-optical implants. In addition, improving from the anti-biofouling properties of high- and moderate-aspect-ratio nanostructures that typically rely on physical cell lysis[12,13,18], we engineered the low-aspect-ratio nanostructures to generate strong nanostructure-mediated hydrophilicity and anti-adhesion barrier for proteins and cellular fouling without inducing cell lysis and inflammation.

To demonstrate the multifunctionality of bio-inspired nanostructures in medical use, we combined the bottom-up nanofabrication approach with top-down microfabrication processes and made a nanostructured micro-optical implant that senses intraocular pressure (IOP) for diagnosis and management of glaucoma, which is a leading cause of irreversible blindness globally[19–21]. We confirmed significant improvement in the bio-inspired

nanostructured sensor's optical readout angle, pressure-sensing performance, and biocompatibility during a one-month *in vivo* study conducted in rabbits.

## Multifunctional nanostructures of *C. faunus* butterfly

The *C. faunus* butterfly (Fig. 1a) belongs to the Riodinidae family found in South America. We have discovered that the *C. faunus* wings are distinct from most other transparent wings in nature[9,11,22]. They have a rare combination of two transparent regions that transmit light differently: (1) the basal transparent areas close to thorax (indicated by a blue arrow in Fig. 1a); and (2) the postdiscal transparent areas further away from the thorax (indicated by a red arrow in Fig. 1a) of both the forewing and hindwing. High-resolution scanning electron microscopy (SEM) of the postdiscal transparent area (Fig. 1c) reveals dome-shaped nanopillars with moderate aspect-ratios (1.090 ± 0.041; Fig. 1b and Supplementary Fig. S1), compared to other natural transparent wings with higher aspect-ratios (>1)[10–12]. Interestingly, the basal transparent area is composed of similarly shaped nanostructures at a lower density (Fig. 1d). The two-dimensional fast Fourier transforms of the SEM images showed ring-shaped distributions (insets of Fig. 1c and 1d), which confirmed their short-range-ordered arrangements[11,23]. The finite diameters of the rings in *k*-space quantified the average periods of the nanostructures as 140–180 nm and 200–300 nm for the postdiscal and basal areas, respectively.

The zone-dependent variation in average inter-structural periods on the *C. faunus* wing plays an important role in the extent of light scattering on the wing. The postdiscal area with an average period below 200 nm remains scattering-free and anti-reflective in the ultraviolet (UV)-visible (VIS)-near-infrared (NIR) regime, and this is well-explained by the effective medium theory and the transfer-matrix model as in other anti-reflective subwavelength nanostructures found in nature[11,24] (Supplementary Fig. S2). The basal area with an average period exceeding 200 nm comparable to light wavelengths shows forward narrow-angle scattering due to more sparsely-located, moderate-aspect-ratio low-index nanostructures[25,26]. Our finite-difference time-domain simulations performed on both groups of nanostructures for 420-nm wavelength produced matching results that confirmed the scattering mechanism of the basal area (Fig. 1e–f). Although we used the same structural height and diameter for both groups in the simulations, the nanostructures with a 150-nm period (similar to the postdiscal area) did not alter the transmitted field (Fig. 1e), whereas nanostructures with a 300-nm period (similar to the basal area) showed forward scattering of the transmitted light (Fig. 1f). The scattering phenomenon of the basal region is moreover confirmed by the difference observed between the specular transmittance and total transmittance in the VIS-NIR range shown in Fig. 1h.

To further analyse the transmissive scattering properties of both areas, we have performed the angle-resolved scattering spectroscopy in the VIS range and varied both the incident and detection angles (Fig. 1i–j). Having almost identical specular and diffuse transmissions in the VIS-NIR range (Fig. 1g), the postdiscal area exhibited specular transmittance with a low scattering angle of ±3° (Fig. 1i). On the other hand, the basal area scattered light in the forward direction with scattering angles up to ±12° and showed negligible changes with incident angle variation, demonstrating its potentially very useful angle-independent

scattering property (Fig. 1j). This scattering property could ameliorate the difficulty of detecting optical signals at wide angles, a commonly observed challenge among many light-based devices[14] such as implantable IOP sensors[15] (See Supplementary Section SI1 and Fig. S3–S4 for more details on the biological significance of the multifunctional transparency and its dual nano-structural basis present on *C. faunus* wings.)

Additionally, the periods of the nanostructures on *C. faunus* wings also influence the wetting properties, and the static contact angles in the postdiscal and basal areas measured 105° and 85°, respectively. The contact angle in the postdiscal area is larger due to the higher surface roughness[27]. In our experiments, these nanostructures with moderate aspect-ratios, similar to nanostructures with high aspect-ratios, resist microbial and cellular growth (Supplementary Fig. S5–S6).

## Development of bio-inspired nanostructured membranes

Inspired by the nanostructures on the basal area of the *C. faunus* wings, we implemented short-range-ordered nanostructures on $Si_3N_4$-membranes (Fig. 2a) by utilizing a highly scalable bottom-up fabrication process based on polymer-phase separation[28,29]. $Si_3N_4$ was chosen for its ease of fabrication on Si and proven performance as an optically transparent and mechanically robust freestanding membrane in microdevices[30,31] as well as for its intrinsic hydrophilicity that is crucial to the antifouling property of the nanostructures as discussed in more detail later in this work.

We created disk-shaped nanostructures with aspect-ratios ranging from 0.15 to 0.90 and performed parametric studies to determine optical and anti-biofouling properties (Supplementary Fig. S7). Nanostructures with an aspect-ratio of 0.45 (Fig. 2b), which was smaller than the aspect-ratio of ≈1 observed in the nanostructures found on the *C. faunus* wings, were found to provide an optimal balance between the anti-biofouling and angle-independent optical properties best-suited for optical implants (see Supplementary Section SI2). Henceforth, the aspect-ratio of nanostructures integrated on the membrane is 0.45 unless stated otherwise.

The SEM image of the nanostructured $Si_3N_4$-membrane is shown in Fig. 2c. The 2D-fast Fourier transform of the SEM image shown in the inset indicates a short-range order with a mean period of 445 ± 60 nm, similar to the periodicity of the basal area. The contact angle on the surface of the nanostructured $Si_3N_4$-membrane was 17°, suggesting an increase in hydrophilicity compared to 38° measured on flat $Si_3N_4$ without nanostructures (Supplementary Fig. S8).

We characterised the optical properties of the nanostructured $Si_3N_4$-membrane using angle-resolved transmission spectroscopy in the VIS-NIR range and compared the results to a flat $Si_3N_4$-membrane without nanostructures (Fig. 2d and e). Using the nanostructures, the angle independence of the $Si_3N_4$-membrane transmission was improved by 50%. 3D simulation of the fabricated structures (Supplementary Fig. S9b) further confirms the improved angle-independent transmittance. This angle-independent transmission results from the isotropic nature of the forward scattering caused by the short-range-ordered nanostructures, which is

irrespective of the incident angle (Fig. 1j). As the total transmission is the combination of ballistic (specular) transmission through the thin membrane and scattered transmission caused by the nanostructures (Supplementary Fig. S10)[32], the angle-independent property of the scattered component decreases the overall angle dependence of the total transmission.

## Biophysical properties of the nanostructured surface

*In vitro* testing compared the adhesion of representative proteins, prokaryotes, and eukaryotes on nanostructured and flat $Si_3N_4$ surfaces with lysine-coated glass slides as positive controls. Flat $Si_3N_4$ is moderately hydrophilic (contact angle: 35–40°) and known to vigorously promote cell adhesion and proliferation due to increased adsorption of proteins when compared to more hydrophilic surfaces (contact angle: <20°)[33,34]. Hence, we further increased the hydrophilicity of the $Si_3N_4$ surface by varying the aspect-ratios of the nanostructures from 0.15 to 0.90 and systematically controlled surface hydrophilicity (Supplementary Fig. S8). Once strong hydrophilicity is achieved (contact angle: <20°), a nanostructure-mediated aqueous barrier forms on the surface and limits protein adsorption and cell adhesion to provide an anti-adhesion property (Supplementary Section SI3, Supplementary Fig. S11 and S16)[6,35,36].

We initially investigated the surface adhesion of two representative proteins: (1) fluorescent-labelled bovine serum albumin for its cardinal role in blood–material interactions[4] and high non-specific binding affinity to the surfaces of biomaterials[37]; and (2) streptavidin for its specific binding affinity to $Si_3N_4$ surfaces[38]. Fluorescence-intensity-based quantification of the adhesion force (Fig. 3a, 4b, and Supplementary Fig. S11) demonstrated adhesion on flat $Si_3N_4$ surfaces was three and two times greater compared with nanostructured $Si_3N_4$ surfaces for albumin and streptavidin, respectively.

We then quantified bacterial adhesion using *E. coli* transformed with the green fluorescent protein (Supplementary Fig. S12). In addition to being a popular prokaryotic model, *E. coli* was chosen for its pathogenic potential to cause gram-negative and often antibiotic-resistant infections on and around implants[39,40]. Bacteria on each surface were quantified through a measure of colony-forming units (CFU) (Fig. 3c) and fluorescence-intensity measurements (Supplementary Fig. S13). Both results indicated significantly lower bacterial adhesion on the nanostructured surface compared to flat $Si_3N_4$. Additionally, the SEM image of individual bacterial cells on the nanostructured surface shows no disruption to their shape, indicating no physical lysis (Supplementary Fig. S14).

The HeLa cell line was chosen as a representative eukaryote for its proven robustness, aggressive growth rate, and adherent nature that prompts its frequent usage in adhesion and cytotoxicity assays[41,42]. After 72 hours, the adherent cell density on the flat $Si_3N_4$ was eight times greater than that on the nanostructured $Si_3N_4$ surface (Fig. 3d & 4e). Next, a mortality ratio, the number of dead cells to the number of living cells, was computed for each surface every 24 hours over a 72-hour period. The difference in the mortality ratios of the two surfaces after 72 hours was not statistically significant (Supplementary Fig. S15), which suggested the nanostructured surfaces inhibited eukaryote adhesion and proliferation without inducing cell death.

These results highlight the advantage of the anti-biofouling approach based on strong hydrophilicity and anti-adhesion properties (Supplementary Fig. S11–S16). High or moderate aspect-ratio nanostructures either with tapered sharp tips or dome-shaped tips as in *C. faunus* display potent geometry-dependent bactericidal properties that induce large stresses and deformation on cell walls regardless of their surface chemical composition[43] and actively promote autogenous lysis when placed in contact with mammalian cells[44]. Such anti-biofouling approaches relying on physical lysis could undesirably damage tissues surrounding implants and elicit inflammation. Supplementary Table S1 shows physical lysis occurs on either natural or synthetic nanostructured surfaces if the aspect-ratio of the nanostructures is 1 or greater. Hence, by keeping the aspect-ratio of the nanostructures at 0.45, the anti-adhesion property was leveraged to prevent biofouling without causing any physical lysis. Additionally, the hydrophilicity of the nanostructured surface originates from surface topology, which may provide better long-term reliability over chemical-treatment methods. (See Supplementary Section SI3 and Fig. S17.)

## Use of nanostructures in intraocular pressure sensing

To demonstrate a medical application of multifunctional nanostructures, we used the nanostructured $Si_3N_4$-membrane as an opto-mechanical sensing element in a microscale implantable IOP sensor, which is a hermetically-sealed, pressure-sensitive, Fabry-Perot (FP) resonator[15]. A flat-surfaced or nanostructured flexible $Si_3N_4$-membrane forms the top surface of the FP-resonator while a mirror-like rigid Si forms the bottom surface. The sensor is optimised in the NIR range for minimum absorption in tissue and water. If the ambient pressure or IOP changes, the membrane will deflect accordingly, and the resulting shift in the resonance wavelength will be captured remotely in reflection (Fig. 4a, Supplementary Fig. S19). In *in vivo* testing, FP-based IOP sensors suffer from narrow readout angles that severely limits sensor practical usability (Supplementary Fig. S20) and biofouling that shortens sensor lifespan[15].

To study the dependence on readout angle $\theta$, we compared the measurements from a nanostructured and a flat-surfaced IOP sensor at 1 atm (Fig. 4b–d). The flat-surfaced sensor produced a maximum resonance shift of 16 nm at incident angle of 12° (Fig. 4b). In contrast, the nanostructured sensor produced shifts of 2 nm at 12° and 5 nm at 30°. Decay in the intensity of reflected resonance was also measured as a function of the incident angle (Fig. 4c). For the flat-surfaced sensor, the intensity decayed to zero when the incident angle reached 12° while the signal from the nanostructured sensor remained detectable until 30°. The IOP-measurement error of the flat-surfaced sensor reached 4.59 mmHg at 12° (Fig. 4d), which is approximately 46% of the physiological IOP range observed in humans (10–20 mmHg) and exceeds the ±1.2 mmHg error range of existing clinical tonometers[45,46]. On the other hand, the IOP-measurement error of the nanostructured sensor was 0.07 and 0.92 mmHg at 12° and 28°, respectively. These results highlight the wide-angle performance of the nanostructured sensor. The nanostructured sensor showed excellent linearity (correlation factor: ~1.00) over the clinical range of interest range from 0 to 30 mmHg when tested in a pressure-controlled chamber interfaced with a digital pressure gauge (Fig. 4e). The maximum readout error was 0.26 mmHg, approximately four times lower than that of the flat-surfaced sensor (1 mmHg).

A nanostructured and a flat-surfaced sensor were implanted individually inside the anterior chambers of two New Zealand white rabbits to investigate *in vivo* optical performance and biocompatibility (Fig. 5a). To examine the stability of sensor measurements, the shift $\Delta\lambda$ of the most prominent peak in each spectrum of the set was computed with respect to the mean of the set (Fig. 5b). The standard deviation (s. d.) of $\Delta\lambda$ of the nanostructured sensor was 0.6 nm as opposed to 1.3 nm observed for the flat-surfaced sensor (Fig. 5c). Additionally, the s. d. of IOP measurements produced using the nanostructured sensor was 0.23 mmHg as opposed to 0.64 and 1.97 mmHg calculated from measurements concurrently obtained using the flat-surfaced sensor and tonometry, respectively (Fig. 5d). The angle independence enhanced by the nanostructure integration improved the stability and accuracy of the optical measurements against potential error sources such as respiratory movements, subtle eye motions, and detector misalignment. Furthermore, indirect IOP measurement techniques such as tonometry are influenced by various factors such as corneal thickness, curvature and biomechanics and are in general more error-prone compared to direct IOP measurement techniques such as implantable sensors[15,47].

Both sensors were retrieved after one month of implantation to quantify cell growth on surface and to assess biocompatibility. We used confocal fluorescence microscopy to determine the extent of tissue growth and cellular viability at the time of retrieval. DAPI was used to localize all constituent cells while Phalloidin, which selectively binds to actin, was used as an indicator of cellular processes and health[48]. Additionally, matrix metalloproteinases-2 (MMP-2) was used as an indicator of inflammation for its role in various inflammatory and repair processes[49].

Fig. 5e and 5f show the top views of the z-stacked multi-channel immunofluorescence images of the flat-surfaced and the nanostructured sensors, respectively. Approximately 59% of the flat-surfaced sensor was covered by tissue, and the presence of a vast filamentous F-actin network (Fig. 5e, in green) indicates healthy tissue growth at the time of extraction. Additionally, MMP-2 (Fig. 5e, in red) was observed over the membrane of the flat-surfaced sensor, which could have triggered the extensive cell migration towards this region. In comparison, approximately 5% of the nanostructured surface was covered by tissue, which was a 12-fold improvement over the flat-surfaced sensor, and there was no detectable MMP-2 signal, suggesting the cell signalling and migration patterns present on the flat-surfaced sensor were absent on the nanostructured sensor. This indicates no inflammation occurred post-implantation and highlights the promising role of the nanostructures towards significantly improving *in vivo* biocompatibility of medical implants.

## Conclusions

Inspired by the short-range-ordered nanostructures found on the wings of the transparent longtail glasswing *C. faunus* butterfly, we engineered the biophotonic nanostructures optimised for use in medical implants. By tuning the key physical dimensions of the nanostructures, we have engineered structurally-induced scattering that expands an optical readout angle and improved antifouling with supressed inflammation suitable for IOP-sensing implants. In Glaucoma, accurate IOP monitoring is the only mainstay of disease diagnosis and management[47], and optical sensing approaches for IOP monitoring have been

promising in terms of miniaturization, energy efficiency and frequency of monitoring[15]; however they also require improvement in readout angle and biocompatibility for practical use. The integration of the nanostructures on an IOP-sensing implant significantly expanded its detection range while reducing mean *in vivo* IOP error by 3-folds. Further, the nanostructures effectively suppressed biofouling and inflammation by 12-folds, resulting in a highly practical implant for long-term IOP monitoring. Further development of our bio-inspired work, including continuous IOP monitoring using mobile devices with an integration of features such as memory-based tracking[50], will improve glaucoma treatment outcomes and lower the risk of visual impairment and blindness. With these promising results, we envisage numerous medical technologies and devices will benefit greatly from the multifunctionality of biophotonic nanostructures.

## Methods

### a. High resolution imaging

Dried wings of *C. faunus*, bought from Bicbugs LLC were coated with a 15 nm gold layer (Lesker Labline E-beam Evaporator, Kurt J. Lesker Company®, USA) before examination by scanning electron microscopy (SEM) (FEI Nova 200 NanoLab Dualbeam, USA) operated at 5 kV.

### b. Topographical analysis

ImageJ (https://imagej.nih.gov/ij/), a public domain and Java-based image processing program tool, was used to perform the statistical analysis of the nanostructure size on the wing membrane and fabricated nanostructured $Si_3N_4$ samples. Every pixel in the images was turned into either black or white using a threshold value that was obtained by calculating the mean intensity value of all the pixels of the same image. Subsequently, the diameters and areas of the nanostructures were computed. The 2-D Fourier power spectra were obtained from SEM images and calculated with a fast Fourier transform algorithm in MATLAB.

### c. Optical simulation

The thin film simulations of flat $Si_3N_4$-membrane and the postdiscal area were calculated analytically using MATLAB[11]. The developed multilayer thin-film calculator is based on matching the boundary conditions for Maxwell's equations. Calculations were first done for individual polarizations and by taking the average afterwards to consider the unpolarized light ((TE+TM)/2) condition.

The optical properties of the basal area nanostructures were numerically simulated with the 2D finite-difference time-domain software (Lumerical Solutions Inc.®, Canada). The transmittance of nanostructured membrane were numerically simulated with the 3D finite element method (FEM) (COMSOL Multiphysics®, USA). In order to simulate exact optical properties of the fabricated nanostructured samples, the measured 3D patterning profile was directly imported from SEM in the simulated model. Periodic boundary conditions in the lateral directions ($x$ and $y$) were applied for the calculations. An incoming plane wave impinging the structures under normal and oblique incidence was used and all calculations were performed with a spatial resolution of 5 nm. In the simulation process, the boundary

conditions of the electromagnetic fields in the vertical (z) direction were set on the perfect matching layer (PML) for the model. The total transmittance was calculated for individual geometries for unpolarised light ((TE + TM)/2) at normal and oblique incident angles by integrating the near-zone scattered power (Poynting vector) over a surface before the bottom PML and afterward normalizing with incident intensity.

### d. Optical spectroscopic analysis

Specular transmission and scattering spectra of the *C. faunus* wings were measured using a custom-built optical goniometric setup. A stabilized Tungsten-Halogen light source (SLS201, ThorLabs, USA) was collimated to form a 500 μm wide parallel incident beam that illuminates the sample at a fixed angle. The specular transmission and forward scattered light was detected at fixed and different angles, respectively, with an angular resolution of 2° and coupled into an optical fibre connected to the spectrometer (Flame, Ocean Optics, USA). All measurements were recorded with an unpolarized light.

The diffuse transmittance measurements were performed using a commercial Cary 5000 Vis/NIR with integrating sphere. All measurements were recorded with unpolarised light. The samples were placed in the middle of the integrating sphere using a vice-type centre-mount and the sample holder was rotated around the vertical axis for angle-resolved measurements. Transmission measurements were normalised to that of the uncovered area of the underlying glass slide.

### e. Biomimetic phase-separation through polymer blends and nanostructure texturing

Poly (methyl methacrylate) (PMMA, $M_w$ = 9590, Polymer Standards Service GmbH, Germany) and polystyrene (PS, $M_w$ = 19100, Polymer Standards Service GmbH, Germany) were dissolved in methyl ethyl ketone (MEK, Sigma-Aldrich Co. LLC, USA) with a mass ratio of 65% and 35%. The concentration of the solutions was kept fixed to 25 mg/ml. Solutions were spin-coated on the substrates with a speed of 3500 rpm and acceleration of 2000 rpm/s for 30 seconds. Relative humidity was maintained between 40% and 50% during the spin coating. The de-mixing of the blend components out of the smooth surface occurred during spin coating itself due to the difference in relative solubility of PS and PMMA in MEK. Schematics of this complete 3D lateral phase separation process in humid condition[28]. When the sample begins to spin, water condensation begins at humidity levels above 35%. A layer of water-rich solution is formed at the air solution interface due to the difference in evaporation rate between water and MEK. Water starts to condense from the air into the solution because of the evaporation of MEK, which decreases the temperature on top below the dew point. Because of the high water concentration, a 3-dimensional phase separation occurs between PS/MEK and PMMA/MEK/water. When the film is completely dried, a purely lateral morphology is formed and the PS islands end with an ellipsoidal shape. The samples were then rinsed in cyclohexane for 2 minutes and dried in a stream of $N_2$ to remove the PS islands. Using the PMMA layer as a template, a 30 nm $Al_2O_3$ hard masking layer was deposited via e-beam evaporation (CHA Industries Mark 40). After lift-off, the $Si_3N_4$ was textured through RIE (Oxford PlasmaLab 100 ICP380) resulting in the nanostructured surface.

### f. Nanostructured membrane and sensor fabrication

The fabrication process flow of the nanostructured membrane and IOP sensor is provided in Fig. S18. The sensor consists of two parts (top and bottom) that were individually batch-fabricated and bonded together using a medical grade epoxy to produce a hermetically sealed miniaturized Fabry-Perot (FP) cavity. (T1) The top substrate fabrication begins with 2 μm-thick $SiO_2$ and 400 nm thick $Si_3N_4$ layers deposited on the top and bottom surfaces of a double-side-polished (DSP) Si wafer (thickness: 300 μm) using thermal oxidation and low pressure chemical vapour deposition (LPCVD), respectively. (T2) The $Si_3N_4$ and $SiO_2$ layers on the top surface of the wafer were completely removed using reactive ion etching (RIE) (Plasmalab System 100 RIE/ICP, Oxford Instruments, Inc.) and buffered oxide etch (BOE). Next, a 300 nm-thick Al oxide ($Al_2O_3$) layer was deposited using an e-beam evaporator (FC-1800 E-Beam Evaporator, Temescal) and patterned the surface using photolithography and BOE. (T3) Using the patterned $Al_2O_3$ layer as a hard mask, the wafer was etched using a Bosch process (Plasmalab System 100 RIE/ICP, Oxford Instruments, Inc.) down to the $SiO_2$ etch stop at the bottom surface of the wafer. (T4) The $SiO_2$ layer was removed through BOE to create freestanding $Si_3N_4$-membranes. The nanostructuring process described in the previous section was used to structure the $Si_3N_4$-membrane. (T5) Individual nanostructured membranes were released from the substrate through photolithography and RIE from the backside. (B1) The bottom substrate fabrication begins with a double-side-polished Si wafer (thickness: 300 μm). (B2) Using a photoresist mask, a precisely controlled 4 μm recess was created through RIE to generate the FP cavity gap. (B3) Next, a 300 nm-thick $Al_2O_3$ layer was deposited using an e-beam evaporator and patterned. (B4) Using a single Bosch process, concentric shallow trenches and a deep trench were etched. The shallow trenches were created to serve as reservoirs during the epoxy bonding process to prevent any of the adhesive from overflowing into the FP cavity. The deep trenches were created for the easy separation of bottom chips (bottom parts of the sensors) from the wafer. (B5) The $Al_2O_3$ masking layer was removed in BOE. Finally, a medical grade epoxy was applied along the sides of the top nanostructured membrane chip and the bottom chip to create a hermetically sealed FP sensor implant.

### g. Nanostructured sensor characterisation

The sensors were placed on a tilt stage, which allows for variation of the incident angle, and were probed by a 20× objective lens interfaced with an NIR light source (HL-2000, Ocean Optics), a mini-spectrometer (Maya200 Pro), Ocean Optics), and a CCD camera (Thorlabs, Inc). For linearity measurements, the sensors were placed in a custom-build pressure-controlled chamber. The hydrostatic pressure was between 0 to 32 mmHg and increased at steps of 0.2 mmHg. The output from the sensors were referenced against a digital pressure gauge (1210 Pressure Sensor, TE Connectivity Ltd.) with an accuracy of ± 0.5%. An in-house IOP detection algorithm on MATLAB was used to rapidly calculate the IOP based on the peak locations of the captured reflection spectra (Supplementary Fig. S15).

### h. Protein adhesion assay

Fluorescently labelled bovine serum albumin (A13100, Thermo Fisher Scientific Inc., Waltham, MA, USA) protein with molecular weight of 66 kDa and streptavidin (S21375,

Thermo Fisher Scientific Inc., Waltham, MA, USA) were used for the protein adsorption studies of the control, flat and nanostructured $Si_3N_4$ samples. The BSA and streptavidin were dissolved separately in phosphate buffered saline (PBS, 10 mM, pH 7.4) to a concentration of 2 mM. The substrates were rinsed with PBS to rehydrate the surfaces. All the sample substrates were then immersed in both protein solutions separately and were incubated at 4°C for 24 h. The samples were then removed from the protein solutions, gently washed three times with PBS, and rinsed once with deionized water to remove the PBS salt. Surface protein adsorption was imaged using a Hamamatsu ORCA-Flash4.0 V2 Digital CMOS camera on a Nikon Eclipse 80i fluorescence microscope with a 10X objective. ImageJ/FIJI (https://imagej.nih.gov/ij/) was used to quantify the protein adsorption data on 12 different imaging areas from each sample. All images were converted into binary images with a fixed threshold to enable sample comparison. Statistical methods used to analyse the data were obtained using Prism (GraphPad Software).

### i. Prokaryote adhesion assay

A culture of chemically competent *E. coli* (Edvotek) was used directly after purchase and transformed with the green fluorescent protein (GFP) expressing and ampicillin-resistant plasmid pFluoroGreen™ (Edvotek) followed by plating on selective agar for overnight (O/N) incubation at 37°C. The bacteria were then inoculated in fresh lysogeny broth (LB) with 100 μg/mL ampicillin and isopropyl-$\beta$-D-thiogalactopyranoside (IPTG) and incubated O/N at 37°C under gentle shaking (250 rpm). Upon recovery, the bacteria were diluted in fresh LB to an $OD_{600}$ – 0.25. Two sets of autoclaved substrates consisting of positive control, flat $Si_3N_4$ and nanostructured $Si_3N_4$ were incubated with 2 mL of the bacterial culture. The sets were used for fluorescence imaging and colony-forming unit (CFU) counts. After 4-hour incubation under gentle shaking (100 rpm), the substrates were washed with 1X PBS and placed in a sonication bath for 15 minutes. The substrates for fluorescence intensity measurements were analyzed using a wide-field epifluorescence microscope (10× objective, Leica DMI 600, Leica AG). For CFU counts, a $10^{-5}$ serial dilution was performed for the control and flat $Si_3N_4$ while a $10^{-4}$ serial dilution was performed for the nanostructured $Si_3N_4$. The bacterial suspension from the substrates were then plated onto 3 selective agar plates per substrate. Statistical methods used to analyse the data were obtained using Prism (GraphPad Software).

### j. Eukaryote adhesion assay

Three sets of autoclaved substrates consisting of positive control, flat $Si_3N_4$, and nanostructured $Si_3N_4$ were incubated in complete Dulbecco's modified Eagle's medium (DMEM) (10% fetal bovine serum (FBS) and 1% 100× penicillin/streptomycin) at 37°C and 5% $CO_2$ for 30 minutes. The medium was then aspirated followed by re-addition of fresh complete DMEM. HeLa cells (ATCC, maintained at low passages to avoid contamination) at a fixed concentration of 250,000 $mL^{-1}$ were seeded on each substrate and measurements were collected at 24-hour time point measurements, three in total. At each 24-hour time point, one set of substrates were incubated in a staining reagent consisting of fresh complete FluoroBrite DMEM (10% FBS, 1% 100× penicillin/streptomycin, 1:1000 Hoechst 33342, and 1:1000 SYTOX green) at 37°C and 5% $CO_2$ for 15 minutes. Hoechst 33342 (excitation/emission ~ 350/461 nm) and SYTOX Green (excitation/emission ~ 554/567 nm) probes

were used to stain the nuclei of adherent HeLa cells on the surfaces under test for live imaging (Fig. 2i). Hoechst 33342 is nonspecific of either dead or live cells and provides an estimate of total adherent cell density, whereas SYTOX Green is impermeant into live cells and functions as an indicator of cell death. The co-localization of the two nucleic acid markers was used to ascertain viability ratios (dead/live) for each surface. For the total adherent cell density measurement, 10 representative images were obtained through wide-field epifluorescence microscopy (10× objective, 2 mm diameter of field area, Leica AG) by scanning a fixed 2 cm × 2 cm substrate of each surface. Using a fixed field area and the representative images, an average adherent cell density (count/mm$^2$) was obtained for each surface. An estimate of viability was computed as an average ratio of number of dead cells and live cells per field-of-view taken over 10 representative images. The co-localization of the two labels yielded the number of dead cells per representative field-of-view. The number of live cells was obtained by subtracting the number of dead cells from the total cell count tagged by Hoechst 33342 alone. The ImageJ/FIJI software was used to perform all required measurements. Statistical methods used to analyse the data were obtained using Prism (GraphPad Software).

### k. *In vivo* IOP measurements

The sensors, mounted on silicone haptics, were folded and inserted into the anterior chamber through a 2.8-mm corneal incision[15]. Upon spontaneous unfolding, the haptics were positioned into the iridocorneal angles. A custom-built hand-held detection system was used for the *in vivo* IOP measurements from the nanostructured IOP sensor. The system was interfaced with a high-resolution NIR mini-spectrometer (Maya200 Pro, Ocean Optics) and a portable tungsten halogen light source (HL-2000, Ocean Optics). To obtain a single IOP measurement, spectra were captured for a 60-seconds period with an integration time of 10 milliseconds per spectrum, resulting in 6000 spectra. Many of these measurements are influenced by naturally induced respiratory and subtle eye motions of the rabbits, which cause the angle of incidence to deviate from normal and increases error. Hence, 100 representative reflection spectra with the highest signal-to-noise ratio (SNR) were chosen out of 6000 spectra and used to calculate the IOP. An in-house IOP detection algorithm on MATLAB was used to rapidly calculate the IOP based on the peak locations of the captured reflection spectra (Fig. S15). Rebound tonometry was performed using a hand-held off-the-shelf system (TonoVet).

### l. Confocal immunofluorescence microscopy sample preparation

Once harvested, the sensors were rinsed in 1× PBS with 0.02% $NaN_3$ and incubated in 4% paraformaldehyde (PFA) for 30 minutes at room temperature (RT) followed by O/N incubation at 4°C. Then, the sensors were rinsed in 1× PBS with 0.02% $NaN_3$ followed by incubation in freshly prepared quenching buffer (1× PBS with 0.02% $NaN_3$ and 50 mM $NH_4Cl$) for 15 minutes at RT. Following quenching, the sensors were rinsed again in 1× PBS with 0.02% $NaN_3$. The sensors were then incubated in blocking buffer (1× PBS with 0.02% $NaN_3$, 2% BSA and 0.25% Triton™ X-100) O/N at RT with gentle shaking (20 rpm). For staining, the sensors were incubated in 1 mL staining reagent containing blocking buffer with 1:1000 DAPI 405 (cell nucleus marker), 1:500 Phalloidin 488 (cell F-actin marker), and 1:500 MMP-2 594 (matrix metalloproteinases marker)) O/N at RT with gentle shaking (20

rpm) followed by 37°C for 1 hour. Following staining, the sensors were washed in blocking buffer several times followed by incubation O/N at RT with gentle shaking (20 rpm). All confocal imaging was performed with the sensors fully immersed in blocking buffer to retain the morphology of the tissue.

### m. Confocal immunofluorescence microscopy and analyses

Imaging for *in vivo* biocompatibility analysis was performed using a laser scanning confocal microscope (LSM 880 with Airyscan, Carl Zeiss AG). Z-stack images (step size: 2.5 μm, range: 500 μm) were captured using a 25× EPI objective with immersion oil, and controlled by Zeiss ZEN 2.1 software. A 2×2 tiling with 10% overlap section of each sensor field of view was captured and then stitched together using an imaging software (Zeiss ZEN, Carl Zeiss AG). All subsequent image analyses were performed with ImageJ/FIJI software.

### o. Ethics

All animals were treated in accordance with the Association for Research in Vision and Ophthalmology (ARVO) Statement for the Use of Animals in Ophthalmic and Vision Research. All animal research was conducted under protocols approved by the Institutional Animal Care and Use Committee of the University of California San Francisco (Protocol no. AN110948).

## Supplementary Material

Refer to Web version on PubMed Central for supplementary material.

## Acknowledgments

The work was funded by the National Institute of Health (NIH) research grant EY024582 to H.C. & D.S., a HMRI Investigator Award, Caltech CI2 program, Powell Foundation Award to H.C., and a Research To Prevent Blindness Innovation Award to D.S. Imaging was performed in the Biological Imaging Facility, with the support of the Caltech Beckman Institute and the Arnold and Mabel Beckman Foundation. We acknowledge support from the Beckman Institute of the California Institute of Technology to the Molecular Materials Research Center.

## References

1. Jiang, G., Zhou, DD. Implantable Neural Prostheses 2: Techniques and Engineering Approaches. Zhou, D., Greenbaum, E., editors. Springer; New York: 2010. p. 27-61.
2. Joung Y-H. Development of Implantable Medical Devices: From an Engineering Perspective. Int. Neurourol. J. 2013; 17:98. [PubMed: 24143287]
3. Canales A, et al. Multifunctional fibers for simultaneous optical, electrical and chemical interrogation of neural circuits in vivo. Nat. Biotechnol. 2015; 33:277–284. [PubMed: 25599177]
4. Leslie DC, et al. A bioinspired omniphobic surface coating on medical devices prevents thrombosis and biofouling. Nat. Biotechnol. 2014; 32:1134–1140. [PubMed: 25306244]
5. Li YQ, Yu T, Yang TY, Zheng LX, Liao K. Bio-Inspired nacre-like composite films based on graphene with superior mechanical, electrical, and biocompatible properties. Adv. Mater. 2012; 24:3426–3431. [PubMed: 22730223]
6. Bixler GD, Bhushan B. Biofouling?: lessons from nature. Philos. Trans. R. Soc. London A Math. Phys. Eng. Sci. 2012; 370:2381–2417.
7. Li L, et al. Multifunctionality of chiton biomineralized armor with an integrated visual system. Science (80–.). 2015; 350:952 LP–956.

8. Liu K, Jiang L. Multifunctional Integration: From Biological to Bio-Inspired Materials. ACS Nano. 2011; 5:6786–6790. [PubMed: 21910442]
9. Huang Y-F, Jen Y-J, Chen L-C, Chen K-H, Chattopadhyay S. Design for Approaching Cicada-Wing Reflectance in Low- and High-Index Biomimetic Nanostructures. ACS Nano. 2015; 9:301–311. [PubMed: 25555063]
10. Ivanova EP, et al. Natural Bactericidal Surfaces: Mechanical Rupture of Pseudomonas aeruginosa Cells by Cicada Wings. Small. 2012; 8:2489–2494. [PubMed: 22674670]
11. Siddique RH, Gomard G, Hölscher H. The role of random nanostructures for the omnidirectional anti-reflection properties of the glasswing butterfly. Nat. Commun. 2015; 6:6909. [PubMed: 25901418]
12. Ivanova EP, et al. Bactericidal activity of black silicon. Nat. Commun. 2013; 4:2838. [PubMed: 24281410]
13. Kim S, et al. Nanostructured Multifunctional Surface with Antireflective and Antimicrobial Characteristics. ACS Appl. Mater. Interfaces. 2015; 7:326–331. [PubMed: 25560094]
14. Nolte DD. Invited Review Article: Review of centrifugal microfluidic and bio-optical disks. Rev. Sci. Instrum. 2009; 80:101101. [PubMed: 19895047]
15. Lee JO, et al. A microscale optical implant for continuous in vivo monitoring of intraocular pressure. Microsystems &Amp; Nanoeng. 2017; 3:17057.
16. Harding JL, Reynolds MM. Combating medical device fouling. Trends Biotechnol. 2014; 32:140–146. [PubMed: 24438709]
17. Araci IE, Su B, Quake SR, Mandel Y. An implantable microfluidic device for self-monitoring of intraocular pressure. Nat. Med. 2014; 20:1074. [PubMed: 25150497]
18. Hasan J, Crawford RJ, Ivanova EP. Antibacterial surfaces?: the quest for a new generation of biomaterials. Trends Biotechnol. 2013; 31:295–304. [PubMed: 23434154]
19. Quigley HA, Broman AT. The number of people with glaucoma worldwide in 2010 and 2020. Br. J. Ophthalmol. 2006; 90:262–267. [PubMed: 16488940]
20. Peters D, Bengtsson B, Heijl A. Lifetime risk of blindness in open-angle glaucoma. Am. J. Ophthalmol. 2013; 156:724–730. [PubMed: 23932216]
21. Tham Y-C, et al. Global prevalence of glaucoma and projections of glaucoma burden through 2040: a systematic review and meta-analysis. Ophthalmology. 2014; 121:2081–2090. [PubMed: 24974815]
22. Hooper IR, Vukusic P, Wootton RJ. Detailed optical study of the transparent wing membranes of the dragonfly Aeshna cyanea. Opt. Express. 2006; 14:4891–7. [PubMed: 19516647]
23. Noh H, et al. How Noniridescent Colors Are Generated by Quasi-ordered Structures of Bird Feathers. Adv. Mater. 2010; 22:2871–2880. [PubMed: 20401903]
24. Raut HK, Ganesh VA, Nair aS, Ramakrishna S. Anti-reflective coatings: A critical, in-depth review. Energy Environ. Sci. 2011; 4:3779.
25. Van de Hulst HC, Twersky V. Light scattering by small particles. Phys. Today. 1957; 10:28–30.
26. Khudiyev T, Huseyinoglu E, Bayindir M. Non-resonant Mie scattering: Emergent optical properties of core-shell polymer nanowires. Sci. Rep. 2014; 4:4607. [PubMed: 24714206]
27. Wanasekara ND, Chalivendra VB. Role of surface roughness on wettability and coefficient of restitution in butterfly wings. Soft Matter. 2011; 7:373.
28. Huang C, et al. Polymer blend lithography: A versatile method to fabricate nanopatterned self-assembled monolayers. Beilstein J. Nanotechnol. 2012; 3:620–8. [PubMed: 23019558]
29. Siddique RH, et al. Bioinspired phase-separated disordered nanostructures for thin photovoltaic absorbers. Sci. Adv. 2017; 3:e1700232. [PubMed: 29057320]
30. Voskerician G, et al. Biocompatibility and biofouling of MEMS drug delivery devices. Biomaterials. 2003; 24:1959–1967. [PubMed: 12615486]
31. Neumann A, et al. Comparative investigation of the biocompatibility of various silicon nitride ceramic qualities in vitro. J. Mater. Sci. Mater. Med. 2004; 15:1135–1140. [PubMed: 15516875]
32. Limonov, MF., Richard, M. Optical properties of photonic structures: interplay of order and disorder. CRC press; 2012.

33. Lee JH, Lee SJ, Khang G, Lee HB. The Effect of Fluid Shear Stress on Endothelial Cell Adhesiveness to Polymer Surfaces with Wettability Gradient. J. Colloid Interface Sci. 2000; 230:84–90. [PubMed: 10998291]
34. Lee JH, Lee HB. A wettability gradient as a tool to study protein adsorption and cell adhesion on polymer surfaces. J. Biomater. Sci. Polym. Ed. 1993; 4:467–481. [PubMed: 8241063]
35. Banerjee I, Pangule RC, Kane RS. Antifouling Coatings: Recent Developments in the Design of Surfaces That Prevent Fouling by Proteins, Bacteria, and Marine Organisms. Adv. Mater. 2011; 23:690–718. [PubMed: 20886559]
36. Peng C, Song S, Fort T. Study of hydration layers near a hydrophilic surface in water through AFM imaging. Surf. Interface Anal. 2006; 38:975–980.
37. An YH, Friedman RJ. Concise review of mechanisms of bacterial adhesion to biomaterial surfaces. J. Biomed. Mater. Res. 1998; 43:338–348. [PubMed: 9730073]
38. Wu P, Hogrebe P, Grainger DW. DNA and protein microarray printing on silicon nitride waveguide surfaces. Biosens. Bioelectron. 2006; 21:1252–1263. [PubMed: 16002276]
39. Crémet L, et al. Orthopaedic-implant infections by Escherichia coli: Molecular and phenotypic analysis of the causative strains. J. Infect. 2012; 64:169–175. [PubMed: 22115736]
40. Hetrick EM, Schoenfisch MH. Reducing implant-related infections: active release strategies. Chem. Soc. Rev. 2006; 35:780. [PubMed: 16936926]
41. Friedrichs J, Helenius J, Muller DJ. Quantifying cellular adhesion to extracellular matrix components by single-cell force spectroscopy. Nat. Protoc. 2010; 5:1353–1361. [PubMed: 20595963]
42. Chang H-H, et al. Cell adhesion as a novel approach to determining the cellular binding motif on the severe acute respiratory syndrome coronavirus spike protein. J. Virol. Methods. 2014; 201:1–6. [PubMed: 24530430]
43. Pogodin S, et al. Biophysical Model of Bacterial Cell Interactions with Nanopatterned Cicada Wing Surfaces. Biophysj. 2013; 104:835–840.
44. Pham VTH, et al. Nanotopography as a trigger for the microscale, autogenous and passive lysis of erythrocytes. J. Mater. Chem. B. 2014; 2:2819–2826.
45. Icare Finland, Oy. Icare Tonometer. at <http://www.icaretonometer.com/>
46. Reichert Inc. Tono-Pen AVIA®. at <http://www.reichert.com/product_details.cfm?pcId=304&skuId=2980&skuTk=1037022486#.WjG21UqnHIU>
47. Weinreb RN, Aung T, Medeiros FA. The pathophysiology and treatment of glaucoma: a review. Jama. 2014; 311:1901–1911. [PubMed: 24825645]
48. Dominguez R, Holmes KC. Actin Structure and Function. Annu. Rev. Biophys. 2011; 40:169–186. [PubMed: 21314430]
49. Parks WC, Wilson CL, Lopez-Boado YS. Matrix metalloproteinases as modulators of inflammation and innate immunity. Nat Rev Immunol. 2004; 4:617–629. [PubMed: 15286728]
50. Fink, W., et al. Optically powered and optically data-transmitting wireless intraocular pressure sensor device. 2004. at <https://www.google.com/patents/US20040116794>

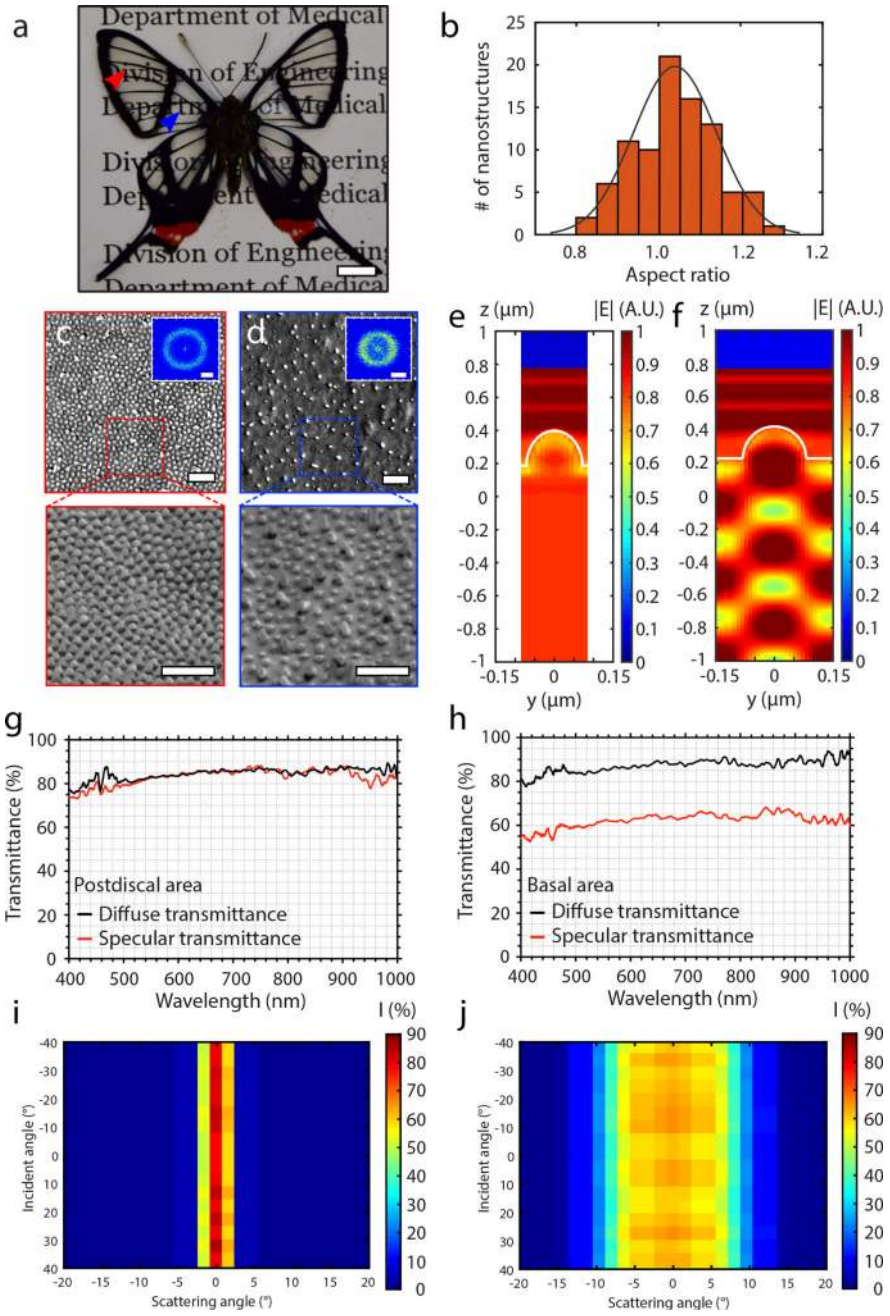


**Figure 1. Characterisation of the *C. faunus* wings**

**a**, Photo of a *C. faunus* butterfly under visible light. The red and blue arrows indicate the postdiscal and basal areas, respectively. Scale bar: 1 cm. **b,** Statistical analysis of the aspect-ratio (height over base diameter) of nanostructures on the *C. faunus* wing. An average aspect-ratio of 1.090 ± 0.041 is estimated by fitting a Gaussian profile. **c, d,** SEM images of the (**c**) densely-packed postdiscal area and (**d**) sparsely-located basal area dome-shaped nanostructures. Insets: 2D Fourier transform of the corresponding nanostructures. Scale bars: 1 μm (inset: 2 $\mu m^{-1}$). **e, f,** Finite-difference time-domain simulations of the near-field scattering profile for the (**e**) postdiscal area (cell periodicity: 150 nm) and (**f**) basal area (cell

periodicity: 300 nm) at the wavelength of 420 nm. **g,** Measured diffuse and specular transmittance of the postdiscal area; difference in spectra within the experimental uncertainty. **h,** Measured diffuse and specular transmittance of the basal area showing a 20% difference in transmittance and a noticeable scattering property. **i, j,** The forward scattering of (**i**) postdiscal and (**j**) basal areas were recorded for a range of incident angles varying from −20 to 20 ° at a wavelength of 420 nm. The measurements depict the different degree of the haze effect for the transparent (low in haze) and translucent (high in haze) areas. The postdiscal area exhibits specular transmittance with a low scattering angle of ±3°. Conversely, the basal area scatters light in a forward direction with a much wider scattering angle of ±12°.

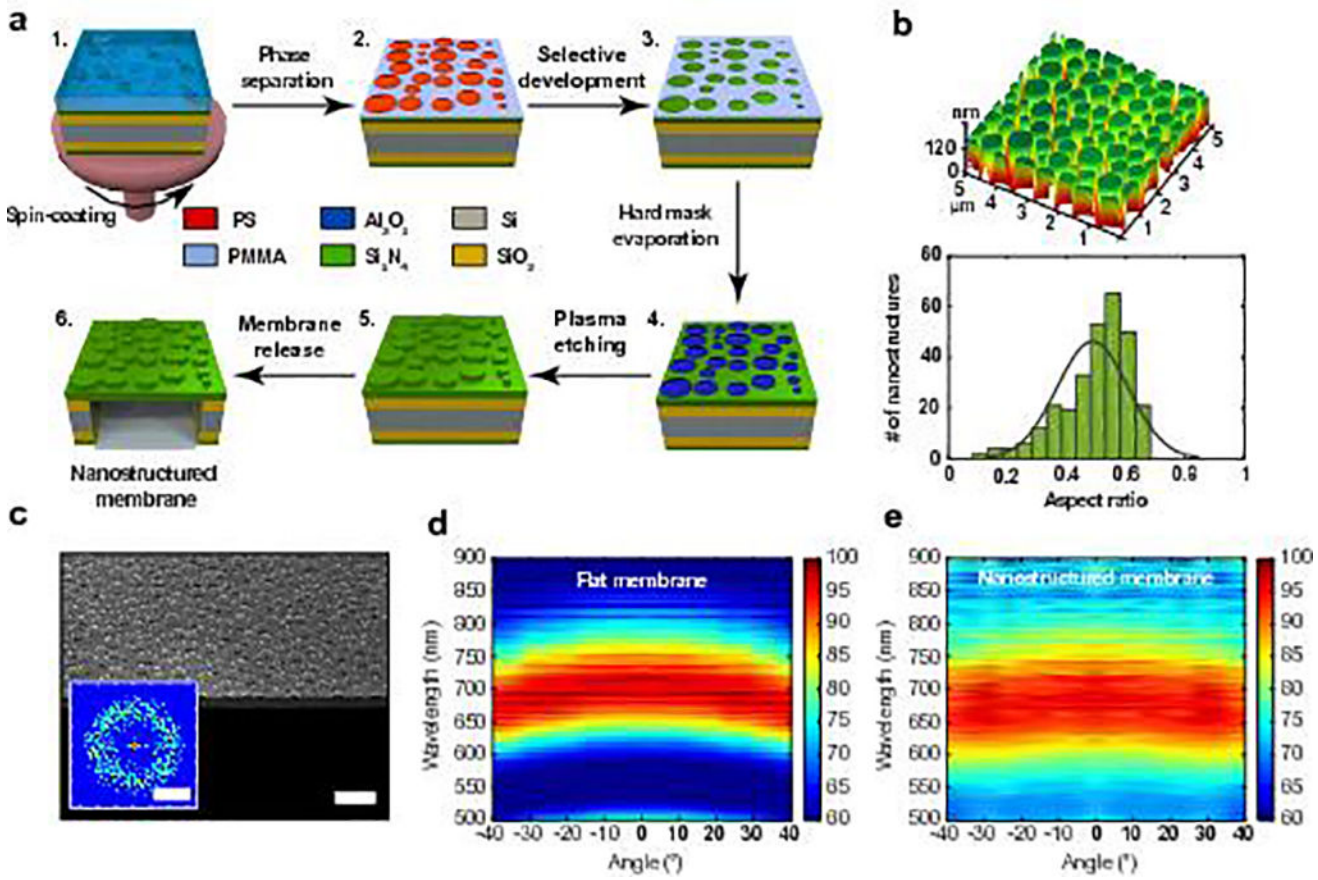


**Figure 2. Nanostructured $Si_3N_4$-membrane fabrication and optical properties**

**a**, The fabrication flow of the bio-inspired nanostructured $Si_3N_4$-membrane: 1. the spin-coating of a blend solution of poly (methyl methacrylate) (PMMA) and polystyrene (PS) in methyl ethyl ketone (MEK) on $Si_3N_4/SiO_2/Si/SiO_2/Si_3N_4$ wafer; 2. phase separation of the polymers; 3. selective development of the PS; 4. $Al_2O_3$ hard mask formation using evaporation and lift-off processes; 5. nanopillar-pattern transfer onto $Si_3N_4$ using plasma etch; and 6. release of the nanostructured $Si_3N_4$-membrane using backside optical lithography and reactive ion etching. **b,** 3D AFM image of the nanostructured $Si_3N_4$-membrane and nanostructure aspect-ratio of 0.450 ± 0.065 approximated with a Gaussian fitting. **c,** SEM image of the nanostructures on the $Si_3N_4$-membrane and corresponding ring-shaped 2D Fourier power spectrum shown in inset. Scale bars: 0.5 μm, inset 1.25 $\mu m^{-1}$. **d,** Experimentally obtained angle-resolved total transmittance of flat $Si_3N_4$-membrane showing a transmission peak around 705 nm due to the light interference introduced by the thin membrane with its peak blue-shifted 30 nm at 40° incident angle due to the angle-dependent nature of the coherent interference process, which agrees with analytical thin-film modelling (Supplementary Fig. S9a), and **e,** experimentally obtained angle-resolved total transmittance of nanostructured $Si_3N_4$-membrane, showing significant reduction in angle-dependence. The integration of nanostructures on the $Si_3N_4$-membrane broadens the total transmission-peak profile, moves its centre from 705 to 685 nm, and limits the magnitude of the peak shift to 15 nm at 40°, compared to 30 nm of a flat $Si_3N_4$-membrane.

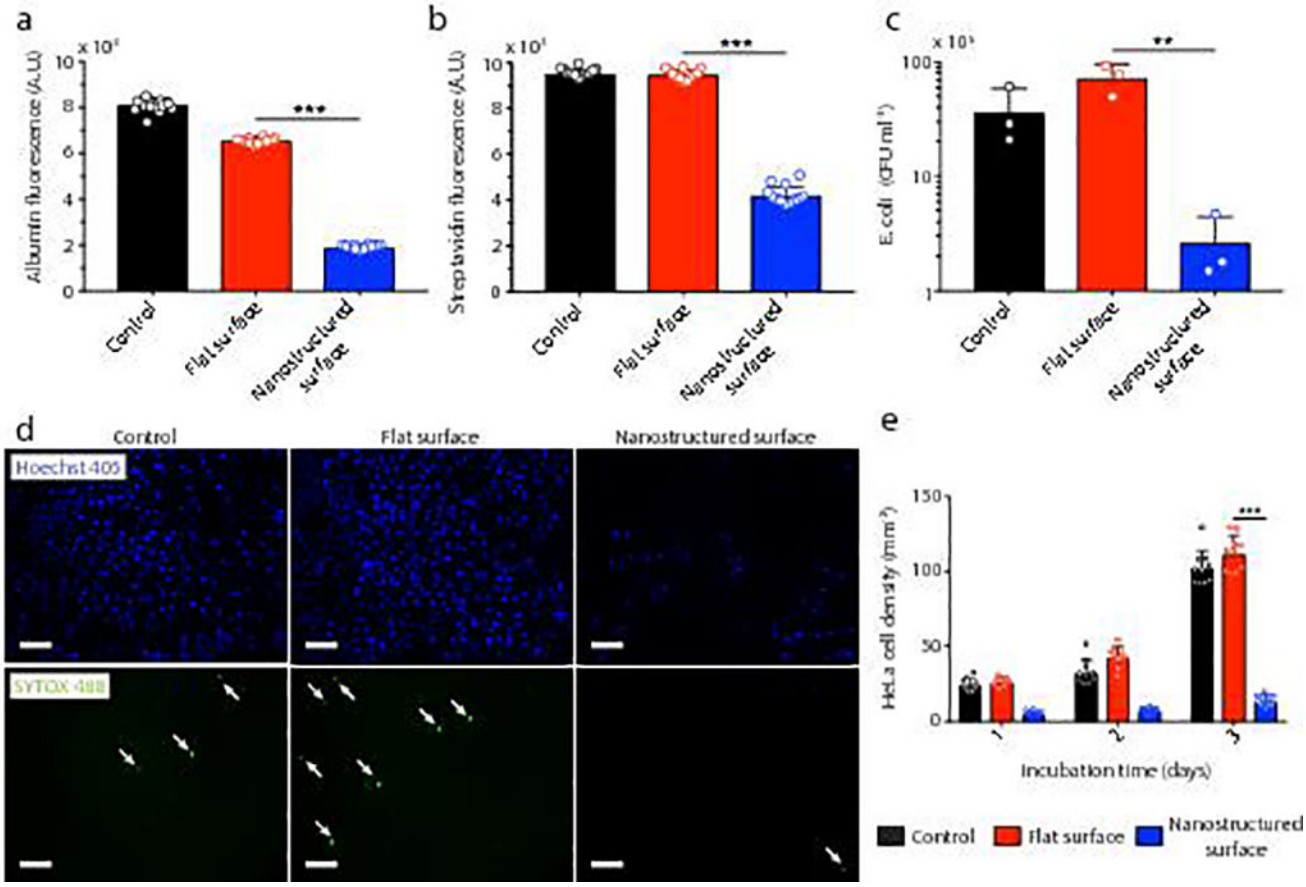


**Figure 3. Nanostructured $Si_3N_4$ surface biophysical properties**

**a, b,** Adhesion force characterised using fluorescence-intensity microscopy for (**a**) bovine serum albumin and (**b**) streptavidin on positive control, flat $Si_3N_4$, and nanostructured $Si_3N_4$ surfaces. Nanostructured $Si_3N_4$ surfaces show significant reduction in albumin and streptavidin adhesion relative to the control and flat $Si_3N_4$ (***$P < 0.001$, one-way ANOVA with post-hoc Tukey test, s.d., $n = 12$ representative images). **c,** The number of adherent CFUs of *E. Coli* on the nanostructured $Si_3N_4$ surface was significantly lower than that on the flat $Si_3N_4$ surface (**$P < 0.01$, one-way ANOVA with post-hoc Tukey test, s.d., $n = 3$ agar plates). **d,** Fluorescent micrographs of a positive control, flat $Si_3N_4$, and nanostructured $Si_3N_4$ incubated for 72 hours in HeLa cell cultures labelled with cell-permeable nucleic acid markers Hoechst 405 (upper panels) and SYTOX Green (lower panels) indicating the anti-adhesive properties nanostructured $Si_3N_4$. The arrows in the micrographs indicate dead cells. Scale bars: 100 μm. **e,** Adherent HeLa cell density on the nanostructured $Si_3N_4$ surface was significantly lower than on the positive control and the flat $Si_3N_4$ surface (***$P < 0.001$, two-way ANOVA with Bonferroni's multiple comparisons test, s.d., $n = 10$ representative images). Adjustments were made for multiple comparisons for all statistical tests used. Experiments (**a**) and (**b**) were replicated three times while (**c**), (**d**) and (**e**) were replicated two times. Error bars are given by the standard deviation about the mean.

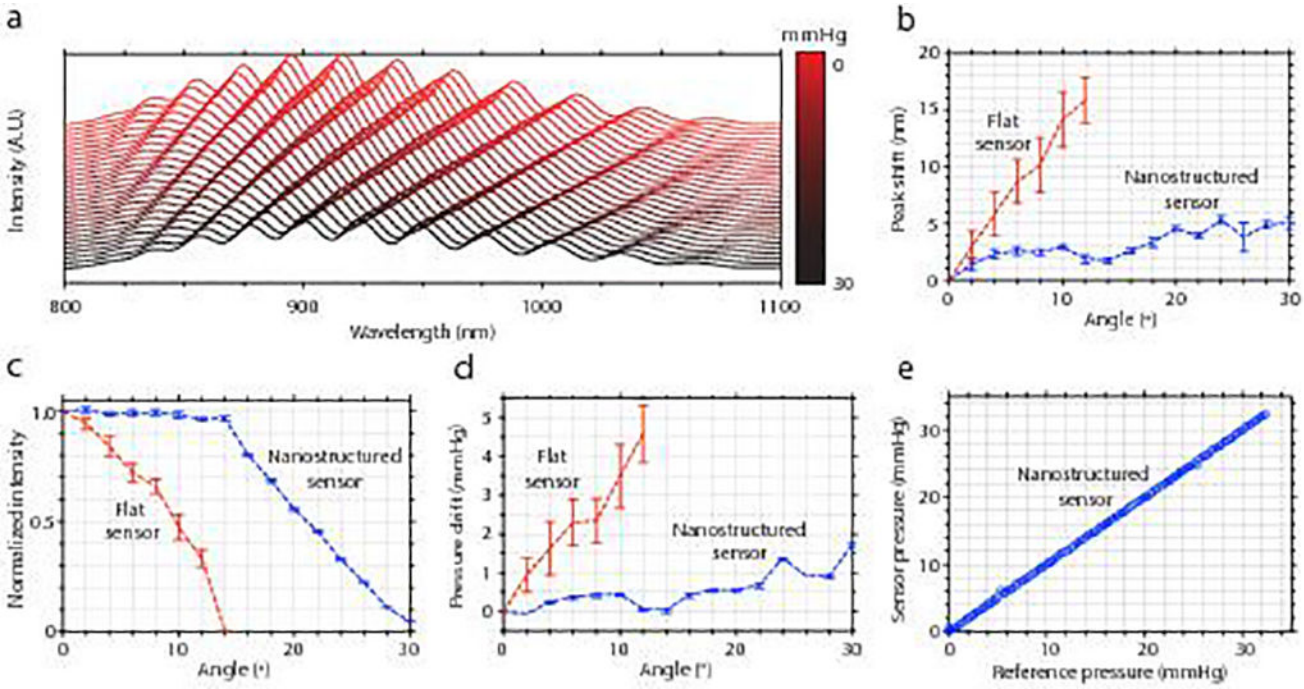


**Figure 4. Benchtop characterisation of nanostructured IOP sensor**

**a**, Resonance shifts of the sensor FP cavity measured in reflection as a function of the IOP. **b,** Peak shift in the reflected resonance spectra as a function of incident angles ($n = 3$ measurements). Considerably smaller magnitudes of peak shifts are observed in the nanostructured sensor, indicating its angle independent property. **c,** Intensity, taken as a measure of peak-to-valley contrast of the most prominent peak and valley of the resonance profile and normalized with respect to the measurement taken at 0° angle of incidence. The nanostructured sensor displays negligible loss of intensity up to 14° ($n = 3$ measurements). **d,** Pressure drift error induced by increasing the angle of incidence. The nanostructured sensor displays negligible pressure drifts even at considerably large angles of incidence ($n = 3$ measurements). **e,** Nanostructured sensor tested from 0 – 32 mmHg in a pressure-controlled chamber interfaced with a digital pressure gauge used as a reference. Error bars are given by the standard deviation about the mean. All the experiments were conducted once.

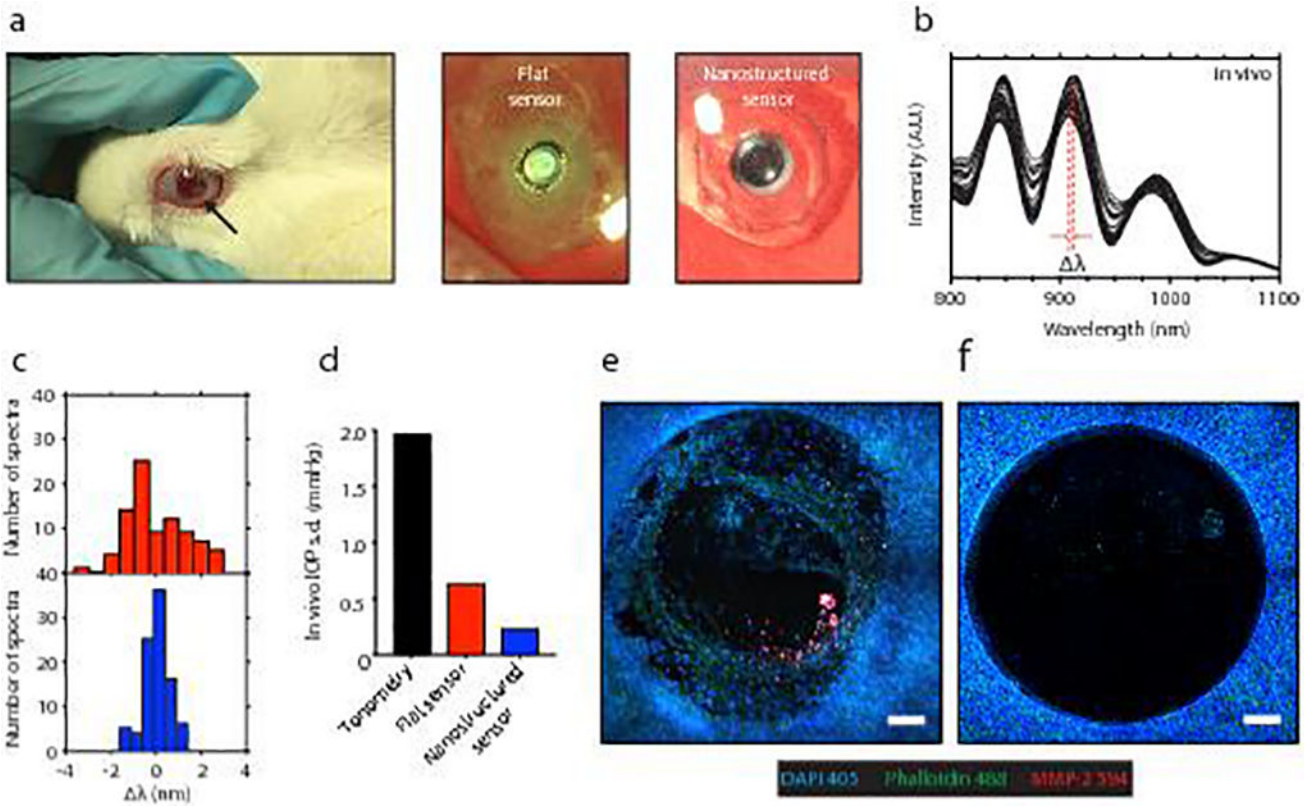


**Figure 5. Nanostructured IOP sensor *in vivo* performance and biocompatibility**

**a**, A flat-surfaced and a nanostructured sensor were each implanted in the anterior chamber of two living New Zealand white rabbits (indicated by black arrow) for a period of 1 month. The sensors were mounted on a flexible silicone haptic and implanted through a minimally invasive surgical process[15]. The flat-surfaced sensor appears hazy compared with the nanostructured sensor due to dense tissue growth on the sensor surface indicating significant biofouling after 1 month of implantation. **b,** Spectra with the highest signal-to-noise ratio (SNR) collected from continual IOP measurements taken over 60-second intervals with an integration time of 10 milliseconds per spectrum. The variation in the position of the resonance spectra that occurred during a single set of measurements is indicated as $\Delta\lambda$ ($n$ = 95 spectra). **c**, Histograms showing the numbers of spectra at specific $\Delta\lambda$ relative to the mean wavelength for the flat (s. d. = 1.3 nm) and nanostructured (s. d. = 0.6 nm) sensors, respectively ($n$ = 95 spectra). **d,** s. d. of *in vivo* IOP measurements made using the flat (s. d. = 0.64 mmHg, $n$ = 95 spectra) and nanostructured (s. d. = 0.23 mmHg, $n$ = 95 spectra) sensors compared with a traditional rebound tonometry reading (s. d. = 1.97 mmHg, $n$ = 12 measurements). **e,** 3-channel immunofluorescence confocal microscopy image (z-stack) of the flat $Si_3N_4$ sensor after 1-month *in vivo* study. Several signs of inflammation (shown in red) over the flat $Si_3N_4$-membrane of the sensor have elicited a foreign body reaction by means of a vast cellular migration process. Healthy tissue growth with a vast F-actin network is observed over the flat $Si_3N_4$-membrane. (DAPI: cell nucleus marker, blue; Phalloidin: cell F-actin marker, green; and MMP-2: matrix metalloproteinases marker, red) **f,** Immunofluorescence image of a nanostructured sensor after 1-month *in vivo* study: Considerably reduced tissue adhesion over the nanostructured $Si_3N_4$-membrane (the circular

region), indicating the contribution of nanostructures to *in vivo* antifouling through anti-adhesion. Experiments (**b**), (**c**) and (**d**) were replicated two times while (**e**) and (**f**) were conducted once.